


Field-driven side-by-side magnetic domain wall dynamics in ferromagnetic nanostrips

Zhoujian Sun¹,* Panpan Fang,¹ Xinwei Shi, X. S. Wang¹,† and Fuxiang Li¹‡
School of Physics and Electronics, Hunan University, Changsha 410082, China

 (Received 9 August 2021; revised 3 June 2022; accepted 5 July 2022; published 18 July 2022)

There has been a plethora of studies on domain wall dynamics in magnetic nanostrips, mainly because of its versatile nonlinear physics and potential applications in data storage devices. However, most of the studies focus on out-of-plane domain walls or in-plane head-to-head (tail-to-tail) domain walls. Here, we numerically study the field-driven dynamics of in-plane side-by-side domain walls in ferromagnetic strips, which can be stable in the presence of an in-plane easy-axis anisotropy transverse to the strip. The domain walls move in a rigid-body manner at low field and show complex Walker breakdown behavior at high field. We observe a multistep Walker breakdown through vortex nucleation in wide strips. In the presence of Dzyaloshinskii-Moriya interaction (DMI), the first Walker breakdown field first decreases then increases with interfacial DMI, while it keeps increasing with bulk DMI. These findings complement the current understanding on domain wall dynamics.

DOI: [10.1103/PhysRevB.106.014412](https://doi.org/10.1103/PhysRevB.106.014412)

I. INTRODUCTION

Over the past few decades, domain wall dynamics has attracted much attention because of the fundamental interest and potential applications in future memory and logic devices [1–3]. Domain walls are transition regions between two differently oriented magnetic domains. The most traditional way to drive the domain wall motion is to apply an external field along one of the domains [4–7]. Later, spin-polarized electric current [8–11], temperature gradient [12–15], and spin waves [16–18] are used as control knobs of domain wall dynamics.

Due to the nonlinear nature of magnetization dynamics, although the field-driven domain wall dynamics has been studied for the longest time, the understanding is still incomplete. On one hand, most analytical models are one-dimensional (1D) models that are only applicable for very thin and narrow lines or strips, or very large bulk systems which are uniform in the other two dimensions [4,19,20]. For generic systems, especially magnetic strips whose width is much larger than the domain wall width, the 1D model fails due to the variation in the width direction [21–23]. On the other hand, most studies focus on in-plane head-to-head (or tail-to-tail) domain walls [15,16] or perpendicular magnetic anisotropy (PMA) domain walls [24–26]. This is mainly because these two types of domain walls are energetically preferable in magnetic nanostrips, which are the platform of domain wall racetrack memory [2]. For soft magnetic materials, the domains align along the strip due to shape anisotropy, forming head-to-head (or tail-to-tail, HtH/TtT for short) domain walls. For materials with strong PMA, the domains are oriented out of plane, and the domain walls between them

are PMA domain walls. However, there is another type of 180° domain wall which is usually ignored, i.e., side-by-side domain walls [27], as schematically depicted in Fig. 1. The magnetization directions of the two domains are in plane and perpendicular to the strip. This type of domain wall may exist in wide strips made of materials with in-plane magnetocrystalline anisotropy, such as cobalt or permalloy grown on some designed substrates [28,29].

There have been a lot of studies on the field-driven dynamics and internal structures of head-to-head (tail-to-tail) domain walls and PMA domain walls [21–23]. It is well-known that in a biaxial system with an easy anisotropy axis and a hard anisotropy axis, the domain wall moves under the longitudinal magnetic field in a rigid-body manner and the velocity increases with the field strength. Beyond a critical field, the rigid-body motion breaks down, and the velocity drops with increasing field. This behavior is called Walker breakdown and the critical field is called Walker breakdown field. For thin strips, the breakdown occurs when the domain wall rotates around the external field [4]. For wide and thick strips, the dynamics is much more complicated. It has been shown that the HtH/TtT or PMA domain walls undergo periodic transformation through the generation and annihilation of vortices [21,22] or Bloch lines [23,30]. In this paper, we theoretically investigate the field-driven dynamics of the third type of domain walls, i.e., in-plane side-by-side domain walls [31]. By micromagnetic simulations, we find a normal Walker breakdown in thin strips which compares well with the 1D analytical model and a multistep Walker breakdown behavior in wide strips. The multistep breakdown occurs due to the generation of vortices and the generation and annihilation of vortex-antivortex pairs. Furthermore, we study the influence of Dzyaloshinskii-Moriya interaction (DMI) on the domain wall dynamics. For bulk DMI (BDMI), the Walker breakdown field increases with BDMI strength. For interfacial DMI (IDMI), the Walker breakdown field first decreases then increases with increasing IDMI strength. These behaviors are

*These authors contributed equally to this work.

†Corresponding author: justicewxs@hnu.edu.cn

‡Corresponding author: fuxiangli@hnu.edu.cn

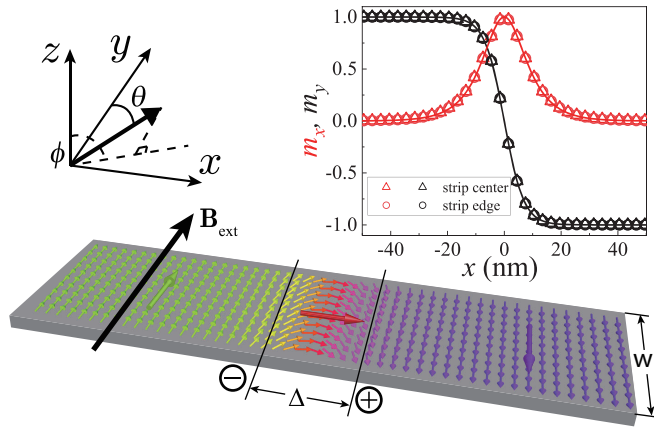


FIG. 1. Schematic illustration of an in-plane side-by-side magnetic domain wall. In the absence of DMI, the static domain wall is Néel type in which all the spins are in plane due to the shape anisotropy. The external field \mathbf{B} is applied along y direction. Inset: Comparison of the m_y and m_x components at the edge and the centerline of the strip.

different from those in HtH/TtT domain walls [32] and PMA domain walls [33] due to the different domain wall geometry. Our findings fill the gap of side-by-side domain wall dynamics and complement the understandings on 180° domain wall dynamics.

II. MODEL AND STATIC SIDE-BY-SIDE DOMAIN WALL

We consider a wide ferromagnetic strip of saturation magnetization M_s along the x direction with easy axis along the y direction of strength K_u , as shown in Fig. 1. The length, width, and thickness of the strip are l , w , and d , respectively. To be convenient, we define a polar coordinate system with respect to y axis.

The magnetization dynamics is governed by the Landau-Lifshitz-Gilbert (LLG) equation [34],

$$\frac{\partial \mathbf{m}}{\partial t} = -\gamma \mathbf{m} \times \mathbf{H}_{\text{eff}} + \alpha \mathbf{m} \times \frac{\partial \mathbf{m}}{\partial t}, \quad (1)$$

where \mathbf{m} is the unit vector of the magnetization direction, γ is the gyromagnetic ratio, and α is the Gilbert damping. The effective field \mathbf{B}_{eff} is the variation of the total energy E , $\mathbf{B}_{\text{eff}} = -\frac{\delta E}{M_s \delta \mathbf{m}}$. We do not consider the DMI at this stage. The total energy density E is

$$E = A|\nabla \mathbf{m}|^2 - K_u m_y^2 - M_s B m_y + E_d, \quad (2)$$

where $A|\nabla \mathbf{m}|^2$ is the exchange energy density with exchange constant A , $-K_u m_y^2$ is the easy-axis anisotropy energy density, $-M_s B m_y$ is the Zeeman energy density with B the field strength along y direction, and E_d is the demagnetization energy density. As a demonstration of concept, we consider ferromagnet strips of thickness $d = 3$ nm with widths w ranging from 48 to 2100 nm and use a moving simulation window of length $l = 3072$ nm centered around the domain wall. The material parameters are $K_u = 2 \times 10^5$ J/m³, $A = 10^{-11}$ J/m, $\alpha = 0.1$, $M_s = 3 \times 10^5$ A/m. The exchange length $L_{\text{ex}} = \sqrt{A/(\mu_0 M_s^2)} \approx 13.3$ nm. In our numerical simulations, we use the MuMax3 [35] package to numerically solve the LLG

Eq. (1) with the mesh size $3 \text{ nm} \times 3 \text{ nm} \times 3 \text{ nm}$, which is smaller than the exchange length.

Due to the thin-film shape anisotropy, the domain wall center should be in plane, resulting in a Néel wall. This can be easily verified by numerical simulation. We set up a $\mathbf{m} \parallel +y$ ($-y$) domain at the left (right) half, and a region of $5L_{\text{ex}}$ wide with random magnetization in between the two domains as the initial state. After relaxing, the domain wall is a Néel-type one as shown in Fig. 1. For $w = 48$ nm, the three components $m_{x,y,z}$ along the strip edge ($y = -w/2$) and the center line ($y = 0$) are plotted in the inset (the origin is set at the center of the strip). It can be observed that the magnetization is almost uniform in the transverse (y) direction, which is different from the strawberry-shape head-to-head walls [21] but similar to the PMA domain walls [25]. The domain wall center can either be $+x$ or $-x$ direction with a degenerated energy in the absence of DMI. The domain wall profile can be well fitted by the Walker solution [4],

$$\theta(x) = 2 \arctan(e^{\frac{x-X}{\Delta}}), \quad \phi(x) = \frac{\pi}{2}, \quad (3)$$

where X is the domain wall center position and Δ is the domain wall width. Here, X is set to 0 and $\Delta = 6.86$ nm from the fitting. In Cartesian coordinates, the solution is $m_y = -\tanh \frac{x-X}{\Delta}$, $m_x = \text{sech} \frac{x-X}{\Delta}$, and $m_z = 0$, as shown by the solid lines in the inset of Fig. 1, showing good agreement with the numerical data points.

The domain wall width Δ is related to A and the effective easy-axis (y axis) anisotropy K_y by $\Delta = \sqrt{\frac{A}{K_y}}$, where K_y includes the magnetocrystalline anisotropy K_u and the shape anisotropy. The shape anisotropy is an approximation of the demagnetization effects, which only considers the homogeneous part of the demagnetization fields and ignores the inhomogeneous part. The effective anisotropy coefficients along y and z axes are $-\frac{N_y - N_x}{2} \mu_0 M_s^2$ and $-\frac{N_z - N_x}{2} \mu_0 M_s^2$, respectively, where $N_{x,y,z}$ are demagnetization factors related to the geometry [36]. In a Néel wall configuration, there are finite bulk magnetic charges $\rho = -M_s \nabla \cdot \mathbf{m}$ at the two sides of the domain wall as schematically labeled in Fig. 1. Thus, the shape anisotropy is approximately that of a prism with dimensions Δ , w , and d [36,37]. The total effective easy-axis anisotropy is $K_y = K_u - [N_y(\Delta, w, d) - N_x(\Delta, w, d)]$ and the total effective hard-axis anisotropy is $K_z = -\frac{N_z - N_x}{2} \mu_0 M_s^2$, which keeps the static domain wall in plane. The domain wall width Δ satisfies

$$\Delta = \sqrt{\frac{A}{K_u - [N_y(\Delta, w, d) - N_x(\Delta, w, d)] \mu_0 M_s^2 / 2}}, \quad (4)$$

where Δ can be self-consistently solved. With our parameters, we have $\Delta = 6.82$ nm, which is quite closed to the numerically fitted value 6.86 nm. The demagnetization factor $N_x - N_y$ increases with the strip width w . Thus, K_{eff} becomes larger and Δ becomes smaller for wider strips, although the change is insignificant because K_u dominates the total K_{eff} .

III. MAGNETIC FIELD DRIVEN DOMAIN WALL DYNAMICS AND MULTI-STEP WALKER BREAKDOWN

We then apply an external field \mathbf{B} along the y direction to investigate the field-driven dynamics of the side-by-side

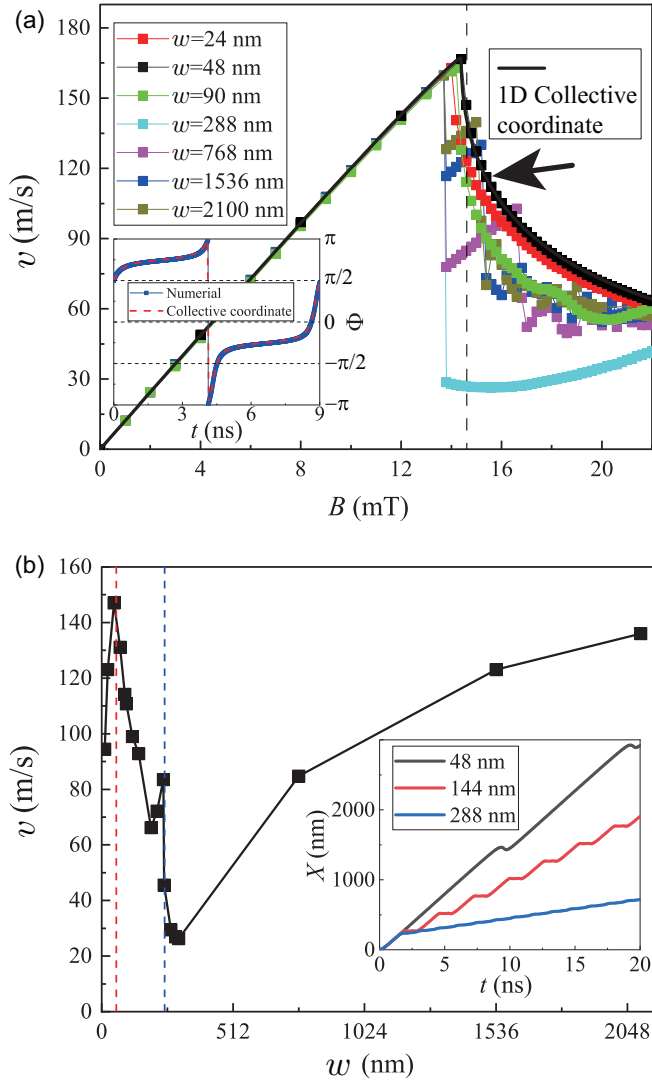


FIG. 2. Domain wall velocity v versus applied field B for different strip width w . The black solid line is the result of collective coordinate model with fitting parameters $K_y = 2.09 \times 10^5 \text{ J/m}^3$ and $K_z = 4.337 \times 10^4 \text{ J/m}^3$ for $w = 48 \text{ nm}$. The inset shows the time evolution of the azimuthal angle Φ of the domain wall plane for $B = 15 \text{ mT}$. The numerical data (thick blue symbols) compares well with the collective coordinate results (red dashed line).

wall. Figure 2(a) shows the domain wall speed v versus the applied field for different strip width w . For thin strips ($w = 24 \text{ nm}$ and 48 nm in the figure), the speed shows a Walker-like behavior [4]: below the Walker breakdown field, the domain wall propagates like a rigid-body; above the Walker breakdown field, the domain wall rotates and oscillates. The average speed in the oscillation regime can be obtained using a well-known 1D collective-coordinate model (CCM) [20,38]. Because of the nonuniform out-of-plane component, the shape anisotropy is no longer a satisfactory approximation. By fitting the $w = 48 \text{ nm}$ curve with the Walker formula and the collective coordinate results [38], we can obtain effective easy-axis anisotropy $K_y = 2.09 \times 10^5 \text{ J/m}^3$ and hard-axis anisotropy $K_z = 4.337 \times 10^4 \text{ J/m}^3$, and the fitted curve shows good agreement with the numerical data. The inset shows the

time evolution of the average domain wall azimuthal angle $\Phi = \arctan\left(\frac{\langle m_x \rangle}{\langle m_z \rangle}\right)$ for $B = 15 \text{ mT}$ (marked by the arrow in the main figure). The good agreement with the 1D CCM means that the side-by-side domain wall dynamics is still quasi-1D at strip width $w = 48 \text{ nm}$.

When the strip width gets wider, the dynamics in the transverse direction becomes more and more inhomogeneous. The way that domain wall chirality periodically flips changes gradually from coherent rotation to vortex generation, and the velocity drop after the Walker breakdown becomes sharper at the same time, which is similar to the well-studied PMA domain walls and HtH/TtT domain walls [21,23,26]. The reason is that the domain wall propagation velocity is proportional to the dissipation rate of the Zeeman energy E_{Zee} , $\frac{dE_{Zee}}{dt} \propto M_s B v$ [39]. When the domain wall moves rigidly, the Zeeman energy dissipation is the only way of energy dissipation. Beyond the Walker breakdown, when the internal dynamics of the domain wall becomes more complex, the Zeeman energy can be temporarily stored in the tilting or deformation of the domain wall. So, the average Zeeman energy dissipation rate becomes lower, resulting in a drop in velocity. However, different from the PMA domain walls [26], the Walker breakdown field does not change much. That is because although the dynamics is not quasi-1D, the Walker breakdown field B_w is still close to the 1D-model value $B_w = \frac{\alpha K_z}{M_s}$. In the side-by-side configuration, the hard axis is dominated by the shape anisotropy $-\frac{N_z(\Delta, w, d) - N_x(\Delta, w, d)}{2} \mu_0 M_s^2$. The change of w in the y direction does not affect this value too much.

We can find more interesting and sophisticated behaviors by observing the details of the dynamics. Figure 2(b) shows the domain wall speed at $B = 14.6 \text{ mT}$ (just beyond the Walker breakdown field) for different strip width w . There are roughly three regions, separated by the red and blue dashed lines. For strips no wider than 48 nm (at the left hand side of the red dashed line), the 1D CCM is approximately valid. Thus, according to the 1D CCM and the effective anisotropy discussed above, the wider the strip, the larger the Walker breakdown field. So the DW velocity increases with the width for a fixed field just above the breakdown field. No vortex is generated and the DW motion is periodic due to the almost synchronized rotation of DW center. The inset of Fig. 2(b) shows how the average domain wall position $\langle X \rangle$ calculated from $\langle X \rangle = \langle m_x \rangle L/2$ [35,41] moves with time. The black line is for $w = 48 \text{ nm}$. In each period, there is a long fast-moving stage in which the velocity equals to the maximum rigid-body velocity at the Walker breakdown. At this stage, the domain wall almost keeps a rigid-body motion with $\Phi \approx \pi/4$, where Φ is the azimuthal angle of the domain wall plane (see Appendix A). There is also a short slow-down stage due to the rotation of the domain wall center. Φ quickly rotates from $\Phi \approx \pi/4$ to $\Phi \approx -\pi/4$ at this stage and the domain wall moves fast again in a new period.

For widths between the red dashed line and blue dashed line, there will be clear vortex generation and propagation, which is similar to that observed in HtH/TtT [21,23] and PMA domain walls [26]. As shown in the inset of Fig. 2(b) by the red line, starting from a Néel wall pointing to $+x$ as shown in Fig. 1, the domain wall still tilts out of plane, shrinks, accelerates, and moves fast with an almost uniform Φ angle at the beginning. But soon, a vortex whose center points to $-z$

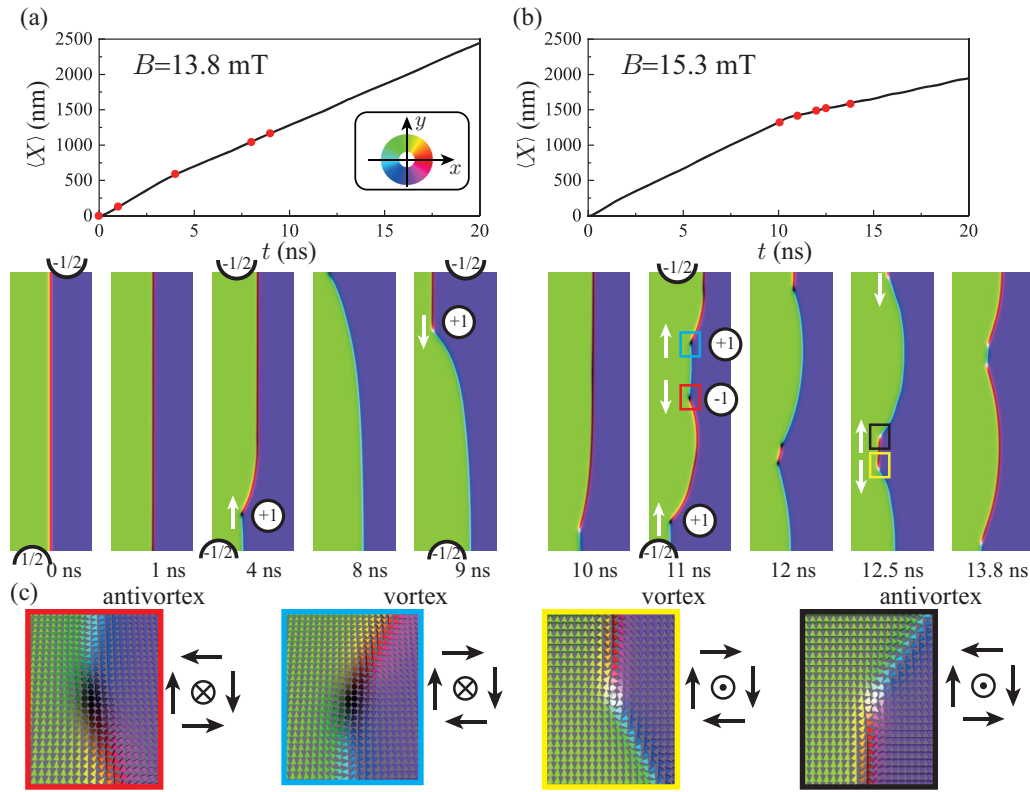


FIG. 3. Upper panel: The average domain wall position $\langle X \rangle$ against time for $w = 1536$ nm and (a) $B = 13.8$ mT, (b) $B = 15.3$ mT. Lower panel: The snapshots of the magnetization texture near the domain wall corresponding to the moments marked by red dots in the upper panel. The in-plane angle of the magnetization is encoded in the color ring shown in the inset. The winding numbers are labeled by circles or semicircles for vortices and edge defects. The moving directions of the vortices are indicated by arrows. Movies for the domain wall dynamics are shown in the Supplemental Material [40]. (c) Close-up textures of the (anti)vortices labeled by frames of different colors in (b). The corresponding schematic spin configuration is schematically illustrated at the right-hand side of each texture.

(polarity $P = -1$) appears at the bottom edge, and the domain wall decelerates. The reason why the vortex appears at the bottom edge is that for the dipolar fields stabilize (destabilize) the $+x$ domain wall center at the top (bottom) edge. So, for the domain wall center point to $-x$, the vortex is generated at the top edge. The Zeeman energy converts to the energy of the vortex and at the same time, the longitudinal motion slows down and wanders around. After the vortex annihilates at the other side, the domain wall moves fast again in the absence of vortex. After a while, a vortex (of opposite polarity) is generated at the top edge, and the motion slows down again. For widths larger than the value indicated by the blue dashed line, there is also vortex generation and the starting stage is similar to the previous case. However, after the vortex annihilates, a new vortex *immediately* appears at almost the same place. There is no fast-moving stage. Thus, the average speed is significantly reduced, as shown in the inset of Fig. 2(b) by the blue line for $w = 288$ nm. This behavior can also be observed in wider domain walls, but the domain wall acceleration and deceleration becomes insignificant. This is because the energy cost of the vortex generation does not scale with the width since it is a local process, while the Zeeman energy is proportional to the width. So the impact of vortex generation on the Zeeman energy changing rate becomes weaker. Figure 3(a) shows the magnetization snapshots of a $w = 1536$ nm strip under $B = 13.8$ mT together with the

average domain wall position $\langle X \rangle$ calculated from $\langle X \rangle = \langle m_x \rangle L/2$ [35,41]. The above-mentioned single vortex generation (annihilation) processes associated with polarity flipping at the strip edges can be clearly seen. For clarity of narration, we call such processes single-vortex processes.

For strips wider than 300 nm, a multistep Walker breakdown can be observed, similar to that in PMA strips [26] [see data for $w = 768$, 1536, and 2100 nm in Fig. 2(a)]. When further increasing the applied field after the first breakdown, a second breakdown occurs with a velocity drop. To see what happens, we plot the magnetization snapshots of the 1536-nm-wide strip under $B = 15.3$ mT, just beyond the second breakdown in Fig. 3(b), and show several typical snapshots of the magnetic texture near the domain wall. During the first ~ 10 ns, the domain wall still undergoes a single-vortex process as depicted above (see the 10 ns snapshot). However, after 10 ns, a vortex-antivortex pair of polarity -1 emerges inside the domain wall (see the 11 ns snapshot). The vortex (antivortex) has a winding number of $+1$ (-1) [42]. The winding number of a vortex is also called vorticity (V). Due to the opposite vorticity and same polarity, the vortex and the antivortex have opposite gyrovectors, so they move along $+y$ and $-y$, respectively, according to the Thiele equation [43,44]. Also due to the finite gyrovectors, the longitudinal speed of the vortex (antivortex) is smaller than the transverse domain wall, so the domain wall speed is slowed down. Then the vortex

hits the top edge, reverses its polarity and moves down. The antivortex annihilates with the other vortex coming up from the bottom edge and a vortex-antivortex pair of polarity +1 emerges at the same place (see the 12 ns and 12.5 ns snapshots). The vortex (antivortex) moves along $-y$ ($+y$), and then hits the bottom edge (annihilate with another vortex), finishing a period. The vortex-antivortex generation and annihilation occur in the interior of the domain wall, and we call them two-vortex processes. Figure 3(c) shows the zoom-in textures near the (anti)vortices labeled by frames of different colors in Fig. 3(b). To see the vorticity and the polarity more clearly, the spin configuration of each texture is schematically illustrated. The red, blue, yellow, and black frames enclose antivortex of polarity -1 , vortex of polarity -1 , vortex of polarity $+1$, and antivortex of polarity $+1$, respectively. Notice that the two-vortex processes in the interior and the single-vortex processes at the edges are asynchronous. So, after time goes on, the vortex-antivortex pair may appear at different positions inside the domain wall and the dynamics may become more and more complicated. We also label the winding numbers of all the vortices ($+1$ for vortices and -1 for antivortices) and edge defects. No matter how complicated the domain wall transformation is, the total winding number remains zero. When B further increases, there can be more pairs of vortices and antivortices. For larger applied field, more two-vortex processes occur at the same time, resulting in further breakdowns. Note that, different from the PMA domain walls [26,45–47] and HtH/TtT domain walls [21], there is no global, directional in-plane tilting of the domain wall centerline (domain wall centerline is the contour line of $m_y = 0$, i.e. the domain wall center). Of course, transient, local tilting near the vortices is ubiquitous, as shown in Figs. 3(a) and 3(b). This is because in the side-by-side geometry, there are no magnetic charges at two ends of the domain wall like those in PMA and HtH/TtT domain walls, so the domain wall width Δ is almost constant along the y direction. For the snapshots shown in Figs. 3(a) and 3(b), the difference between the smallest and largest Δ is less than 3%.

IV. INFLUENCE OF DZYALOSHINSKII-MORIYA INTERACTION

As an antisymmetric exchange interaction, DMI has been demonstrated to have a significant influence on HtH/TtT [32] and PMA [25,33] domain wall dynamics. There are two most widely studied types of DMI, i.e., the interfacial DMI (IDMI) and the bulk DMI (BDMI). The interfacial DMI exists in inversion symmetry breaking systems. The DMI vector direction $\hat{\mathbf{d}}_{12}$ from spin 1 to spin 2 is parallel to $\mathbf{r}_{12} \times \hat{\mathbf{z}}$, where \mathbf{r}_{12} is the spatial vector from 1 to 2 and $\hat{\mathbf{z}}$ is the inversion symmetry breaking direction [33]. The bulk DMI exists in noncentrosymmetric systems. $\hat{\mathbf{d}}_{12}$ is parallel to \mathbf{r}_{12} [48]. The DMI vector directions are schematically illustrated in Fig. 4. For static domain wall configurations, it is enough to use the simplest three-spin model to decide the energetically preferred configuration in quasi-1D. Figure 4 summarizes the influence of the two types of DMI on different types of domain walls. The side-by-side walls are different from the HtH/TtT walls and PMA walls. The IDMI does not break the degeneracy of the Néel type (domain wall center in-plane) and the Bloch

$\odot \hat{\mathbf{z}}$	HtH/TtT	Side by Side	PMA
IDMI 			
BDMI 			

FIG. 4. Schematic diagrams of interfacial and bulk DMI and summary of energetically preferred static domain wall configurations. The check mark (cross mark) means the configuration is preferable (not preferable). The circle means that the DMI has no influence on the static domain wall configuration.

type (domain wall center out-of-plane). The BDMI prefers the Bloch type, which is competing with the shape anisotropy. In the continuous model, the expressions of energy density of IDMI and BDMI are, respectively,

$$E_{\text{IDMI}} = D_i [m_z \nabla \cdot \mathbf{m} - (\mathbf{m} \cdot \nabla) m_z], \quad (5)$$

$$E_{\text{BDMI}} = D_b \mathbf{m} \cdot (\nabla \times \mathbf{m}), \quad (6)$$

where D_i and D_b are the IDMI and BDMI strength in units of J/m^2 . Applying the quasi-1D $X - \Phi$ CCM Eq. (A7), we find the total energy \mathcal{E} of the side-by-side domain wall in the presence of IDMI or BDMI (see Appendix):

$$\mathcal{E}_{\text{IDMI}} = 4dw \sqrt{A(K_y + K_z \cos^2 \Phi)}, \quad (7)$$

$$\mathcal{E}_{\text{BDMI}} = dw [4\sqrt{A(K_y + K_z \cos^2 \Phi)} - \pi D_b \cos \Phi]. \quad (8)$$

We first focus on the influence of BDMI. For the static domain wall configuration, minimizing $\mathcal{E}_{\text{BDMI}}$ with respect to Φ , we find

$$\cos \Phi = \begin{cases} \pi D_b \sqrt{\frac{K_y}{K_z(16AK_z - \pi^2 D_b^2)}} & |D_b| < D_c \\ \text{sign}(D_b) & |D_b| \geq D_c, \end{cases} \quad (9)$$

where $D_c = \frac{4K_z}{\pi} \sqrt{\frac{A}{K_y + K_z}}$. For $w = 48$ nm, with $K_y = 2.09 \times 10^5 \text{ J}/\text{m}^3$ and $K_z = 4.337 \times 10^4 \text{ J}/\text{m}^3$ obtained in the previous section, we have $D_c = 0.348 \text{ mJ}/\text{m}^2$. From $D_b = 0$ to $D_b = D_c$, the static domain wall gradually rotates from Néel type ($\Phi = \pm\pi/2$) to Bloch type ($\Phi = 0$ for positive D_b and $\Phi = \pi$ for negative D_b). Figure 5(a) shows the quasi-1D result Eq. (9) together with the numerical results, showing a reasonably good agreement.

Then we investigate the field-driven dynamics of side-by-side domain walls in the presence of BDMI. We have discussed that the BDMI tends to lock the domain wall in Bloch type [$D_b > 0$ (< 0) for domain wall center pointing to $+z$ ($-z$)]. Thus, when an external field is applied, the domain wall rotation is suppressed so the Walker breakdown is postponed. Figure 5(b) shows how the average domain

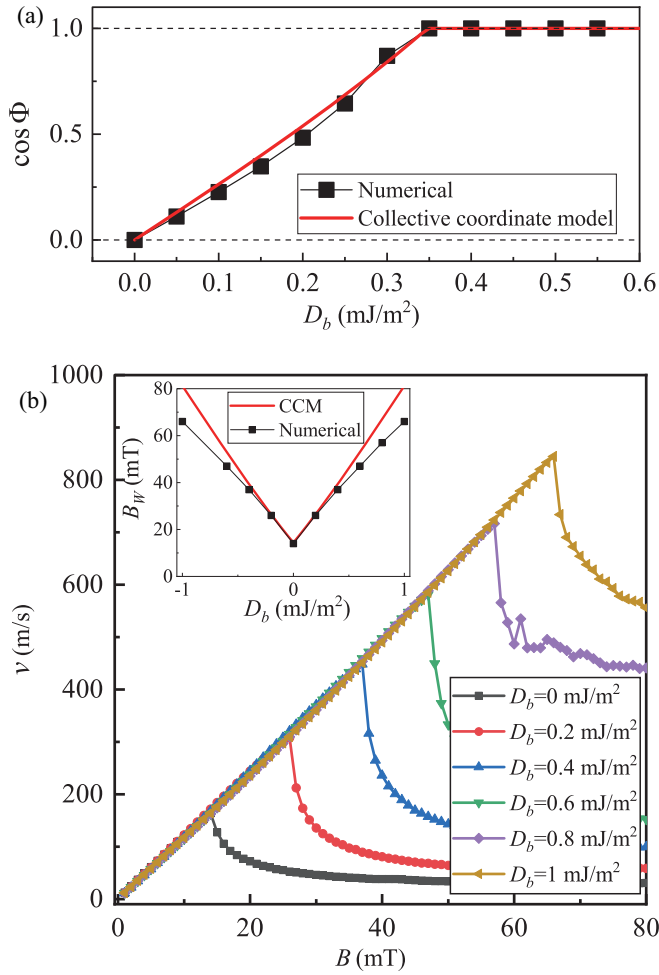


FIG. 5. (a) Influence of BDMI strength D_b on domain wall azimuthal angle Φ . The symbols are numerical data and the solid line is the collective coordinate model result. (b) The simulation results of field-driven domain wall velocity for $w = 48$ nm and different D_b . The inset shows the Walker breakdown field B_W versus D_b . The symbols are numerical data and the solid line is the collective coordinate model result.

wall velocity changes with external field for the 48 nm strip. Typical Walker breakdown behaviors are observed. The breakdown field B_W increases with D_b . The breakdown fields B_W for different D_b are plotted in the inset. The black symbols are the numerical results extracted from the main figure and the red line is the result of 1D CCM (see Appendix). The numerical results qualitatively compare well with the 1D CCM model but the B_W values are smaller, mainly due to the 2D nature and the complicated demagnetization field in the numerical model. Both the CCM model and numerical data show that the domain wall velocity is symmetric for positive and negative D_b .

We now consider IDMI. According to Eq. (7), the IDMI does not affect the static domain wall configuration in 1D model. For a 2D strip of $w = 48$ nm, this is still true for weak IDMI such as $D_i = 0.5$ mJ/m². However, the numerical relaxation shows that the static domain wall centerline is tilted in plane, and the magnetization is tilted out of plane, as shown in Fig. 6(a) for $D_i = 1$ mJ/m². The tilting direction of the

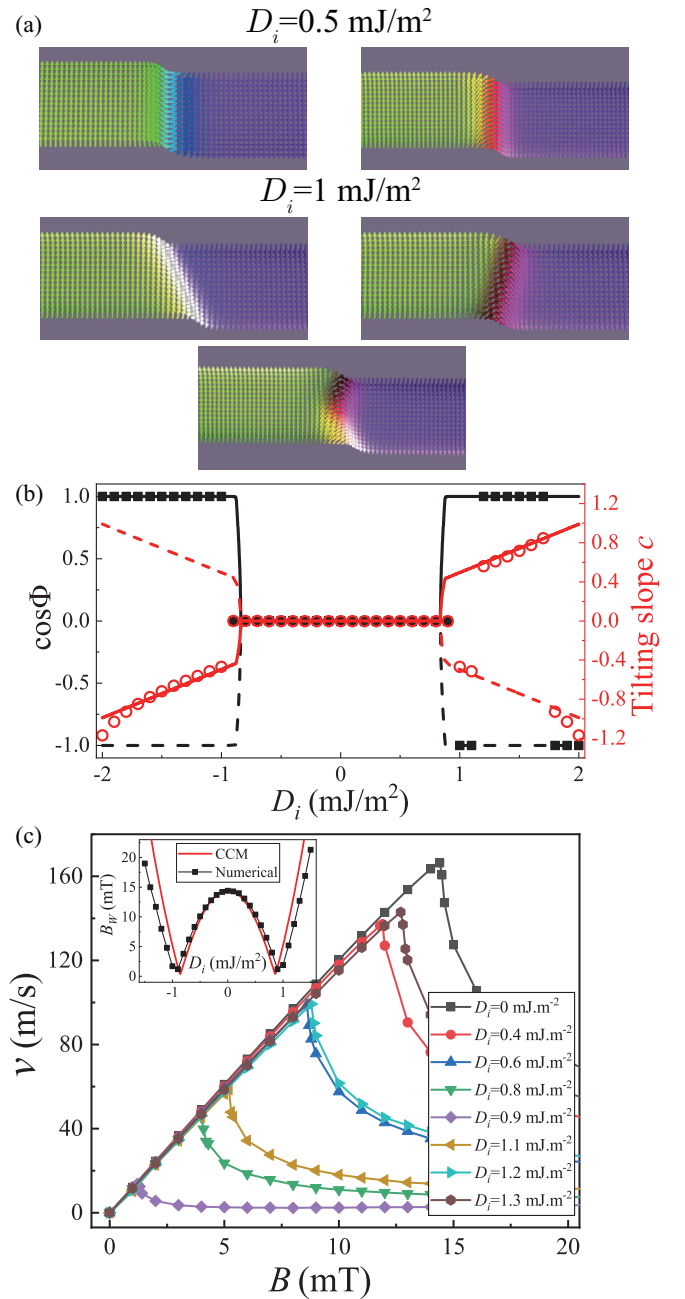


FIG. 6. (a) Static domain wall configuration for $w = 48$ nm and $D_i = 0.5$ (first row) and 1 mJ/m² (second row) numerically relaxed from different random initial states. (b) $\cos \Phi$ of domain wall plane (left axis) and tilting slope c of domain wall centerline (right axis). The symbols are numerical data and the lines are 2D CCM results. The solid lines and dashed lines are two possible combinations of $\cos \Phi$ and c . (c) Field-driven domain wall velocity for different D_i . Inset: Walker breakdown field B_W versus D_i . Symbols are numerical data and the solid line comes from the 2D CCM.

domain wall centerline is correlated with the tilting direction of the magnetization. For $D_i > 0$, when the domain wall centerline lies in the first and third (second and fourth) quadrants, the domain wall magnetization is tilted to $-z$ ($+z$). The probability of the two tilting directions is the same for different random initial states. For some initial states, it is also possible to have more complicated domain wall texture, such as that

shown in the third panel of Fig. 6(a). Different segments of the domain wall tilt to different directions. Such DMI-induced tilting has been observed in PMA domain walls [45–47]. To explain the tilting, we have to introduce a 2D CCM, allowing X to be dependent on y , $X = X(y, t)$. We assume the tilting is linear so $\frac{dX}{dt} = c$ is constant. The static domain wall energy is

$$\mathcal{E}_{\text{IDMI}} = dw[2(2 + c^2)\sqrt{A(K_y + K_z \cos^2 \Phi)} + \pi c D_i \cos \Phi]. \quad (10)$$

The first term in the bracket is related to the balance between exchange energy and anisotropy energy. The larger the tilting, the longer the domain wall, so the first term prefers smaller c . The second term is related to the IDMI. Only when this term is negative can the tilted domain wall be possibly preferred. $\mathcal{E}_{\text{IDMI}}$ can be minimized with respect to c and Φ . For $D_i > 0$, there are two degenerated minimal points, corresponding to $c > 0$, $\Phi > \pi/2$ and $c < 0$, $\Phi < \pi/2$, respectively, which is consistent with the numerical results. Figure 6(b) plots the domain wall azimuthal angle $\cos \Phi$ (left axis) and the tilting slope c (right axis), showing the comparison between numerical data and the CCM model. The solid lines and the dashed lines represent the two ways of tilting with the same energy. The numerical data almost fall on either the solid lines or the dashed lines. When applying an external field, the side-by-side domain wall dynamics shows more interesting behaviors in the presence of IDMI. Figure 6(c) exhibits the domain wall velocity versus applied field for different D_i . The Walker breakdown field B_W first decreases, then increases with D_i , which is different from the HtH/TtT and PMA domain walls. This phenomena can also be understood using the 2D CCM. For small D_i , the straight Néel domain wall is still the ground state and the tilted domain wall only has slightly higher energy. Their energy difference plays a role of a low energy barrier. When D_i increases, the energy of the tilted domain wall becomes lower, so the domain wall is easier to flip between the two Néel configurations, leading to a lower B_W . After a certain value of D_i , the tilted domain wall becomes the ground state and the energy barrier becomes higher when further increasing D_i . Thus, the flipping of the domain wall center becomes more difficult and B_W increases. The inset of Fig. 6(c) shows B_W from numerical data and the CCM result is plotted in solid line for comparison. The simulation and CCM agree well with each other. However, the CCM indicates a symmetrical B_W in positive and negative sides of D_i , but the numerical results are asymmetric. B_W for $-|D_i|$ is always slightly smaller than that for $+|D_i|$. This qualitative discrepancy is mainly due to the IDMI-induced tilting of magnetization at the two side edges of the strip. We recall the finding in Sec. III that for $B > 0$, the inhomogeneous flipping of the domain wall center always starts at the bottom edge. This is also true in the presence of DMI. For positive D_i , at the bottom edge, the magnetization in the left (right) domain is tilted towards $-z$ ($+z$) to minimize the IDMI energy [this can be observed in Fig. 6(a)]. This tilting is clockwise with respect to the $+y$ direction, which is opposite to the counterclockwise torque induced by B . Thus, the bottom edge is relatively robust so a larger field is required to flip the magnetization inside the domain wall. On the contrary, for

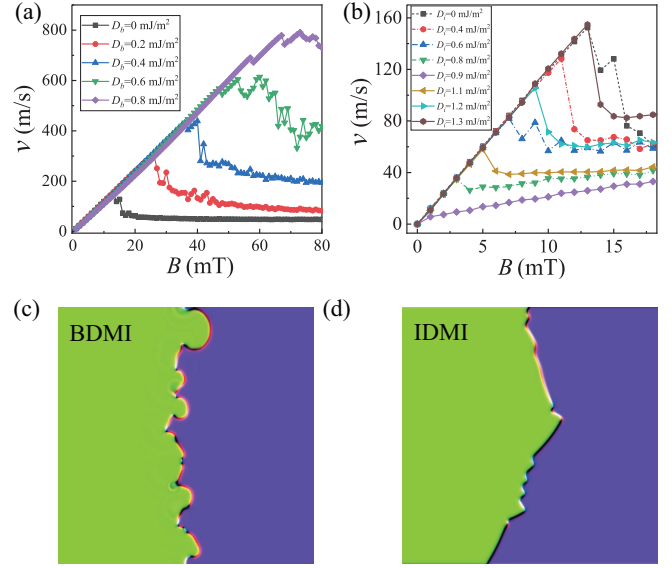


FIG. 7. Domain wall velocity v versus external field B for 1536 nm strip in the presence of different (a) BDMI, (b) IDMI. Typical domain wall texture after Walker breakdown for (c) BDMI, $D_b = 0.8$ mJ/m² and $B = 150$ mT, (d) IDMI, $D_i = 1.3$ mJ/m² and $B = 15.2$ mT.

negative D_i , the tilting is along the same direction as the torque of B . So, the breakdown field is smaller. Since the tilting at the edge is small, this difference in B_W is subtle. For larger $|D_i|$, the difference becomes more significant.

We also perform simulations for wider strips in the presence of BDMI and IDMI. Figure 7 shows the field-driven domain wall velocity for $w = 1536$ nm. Before the Walker breakdown, the dynamics does not differ too much from the 48 nm strip, except the breakdown field becomes smaller. After the Walker breakdown, the dynamics affected by BDMI and IDMI are distinct.

In the presence of BDMI, the energy degeneracy of two chiralities is broken and the system can be mapped to the well-studied PMA domain walls by a $\pi/2$ rotation of \mathbf{m} around x . Thus, we also observe solitonlike domain wall motion similar to that of PMA domain wall described in Ref. [30]. A typical domain wall texture is shown in Fig. 7(c) for $w = 1536$ nm, $D_b = 0.8$ mJ/m², and $B = 150$ mT. The snapshot is taken at $t = 1$ ns. A tortuous domain wall centerline with many vortices can be observed. The vortex generation and annihilation are similar to the Bloch line in PMA domain wall [30]. The suppression of Walker breakdown is also present for D_b larger than 1 mJ/m². More details are discussed in Appendix C.

The IDMI has a totally different affect on the domain wall dynamics. Figure 7(d) shows a typical domain wall texture for $w = 1536$ nm, $D_b = 1.3$ mJ/m², and $B = 15.2$ mT. Different from the curled, tortuous domain wall in the BDMI case, the domain wall centerline is zigzag with each segment straight and the magnetization is out-of-plane for each segment. The tilting direction follows the same rule as the static case discussed above. Compared to the fast (~ 0.1 ns) vortex dynamics in the BDMI case, the zigzag domain wall deforms slowly. New zigzags appear at the edges and gradually annihilate at the middle. Since the dynamics in the presence of DMI is quite complicated, we will study it in a statistical way in the future.

V. DISCUSSION

In the calculations above, we use a large anisotropy K_u so the domain wall is thin (~ 7 nm) to avoid the influence of finite strip length as much as possible. The validity of the continuous model can be demonstrated by comparing the numerical domain wall profile with the Walker solution (the inset of Fig. 1). Furthermore, the threshold domain wall width between the continuous domain wall and abrupt domain wall is $\Delta = \sqrt{3}a/2$, where a is the lattice constant (the mesh size in our case) [49,50]. Our domain wall width is above this threshold. For wider domain walls, our results are still qualitatively correct.

We have explained the observed dynamics in the energy point of view. The Zeeman energy is dissipated via Gilbert damping, leading to propagation of the domain wall, and the transit vortex generation processes temporarily store the Zeeman energy, leading to the change in domain wall speed. We should note that the energy argument can only give an overall understanding but cannot give the detailed dynamics. For weak field below the Walker breakdown, the Zeeman energy can be solely dissipated through Gilbert damping, so the magnetic texture is able to keep unchanged, resulting in the rigid-body motion. When the field is close to or slightly larger than the Walker breakdown, spin wave emission may occur to dissipate more energy [7,51]. For larger field, the domain wall starts to rotate (in thin strips) or nucleate vortices (in wider strips). The Zeeman energy is periodically stored and released by the domain wall, as we have discussed above. For even larger field (larger than the effective field of the easy-axis anisotropy), the domain opposite to the field becomes unstable and more complicated textures emerge, such as another pair of domain walls. In different situations, the Zeeman energy dissipates and converts in different ways. Analyses on the LLG equation are still necessary to know the specific dynamics.

Materials with in-plane uniaxial anisotropy are necessary to experimentally observe and investigate the side-by-side domain walls. The anisotropy K_u should overcome the in-plane shape anisotropy $(N_y - N_x)\mu_0 M_s^2$. It has been observed that cobalt can possess such K_u [28]. The growing condition or external strain can also induce an in-plane uniaxial anisotropy [29,52]. The IDMI may be present in such materials by designing inversion-symmetry structures. It is also possible to induce in-plane uniaxial anisotropy by strain in BDMI materials [53]. Of course, we have studied an ideal theoretical model here. Finite-temperature, geometrical defects like edge roughness and surface roughness, and material defects (including inhomogeneity of material parameters) would exist in reality. They will be the topics of further theoretical studies. In the Appendixes, we briefly discuss the influence of inhomogeneous K_u , which is supposed to be ubiquitous in imperfect materials.

VI. SUMMARY

We investigate the static and dynamic properties of side-by-side domain walls. Although the observed side-to-side domain wall dynamics has many similarities to the HtH/TtT and PMA domain walls, there still exist important differences due to the different geometries. In the absence of DMI,

the domain wall is in Néel configuration due to the shape anisotropy and the domain wall width Δ can be estimated self-consistently using the shape anisotropy of a prism of dimensions (Δ, w, d) . The field-driven domain wall dynamics in thin strips can still be described by the 1D CCM. In wide strips, complicated multistep breakdown behavior occurs via generation, propagation, and annihilation of (anti)vortices. Due to the absence of magnetic charges at the ends of the domain wall, the side-by-side domain wall width is more homogeneous than the other two kinds of domain walls, and there is no directional tilting. In the presence of BDMI, the Walker breakdown field increases with the BDMI so the fast rigid-body domain wall motion is enhanced. The simulation results for thin strips can be well reproduced by the 1D CCM. In the presence of IDMI, domain wall tilting occurs at strong IDMI. The Walker breakdown field first decreases and then increases with the IDMI strength. The nonmonotonic dependence of the breakdown field on IDMI as well as the domain wall tilting can be explained by the 2D CCM. Furthermore, the breakdown field shows subtle asymmetry in positive and negative IDMI, mainly due to the IDMI-induced magnetization tilting at the strip edges. For wider strips, in the presence of BDMI, the domain wall is tortuous with plenty of vortex generation and annihilation. Solitonlike dynamics similar to the PMA domain wall case is observed. In the presence of IDMI, the domain wall becomes zigzag. Our results provide more comprehensive understandings on the properties of domain walls.

ACKNOWLEDGMENTS

This work is supported by the Fundamental Research Funds for the Central Universities. X.S.W. acknowledges support from the Natural Science Foundation of China (NSFC) (Grants No. 11804045 and No. 12174093). F.X.L. acknowledges support from the Natural Science Foundation of China (NSFC) (Grant No. 11905054).

APPENDIX A: COLLECTIVE COORDINATE MODEL

The CCM has been comprehensively studied in previous research [20,33,38,45]. Here we emphasize what are different in side-by-side domain walls. As depicted in Fig. 1, we define the spherical coordinate with respect to y axis for convenience, so $m_y = \cos \theta$, $m_z = \sin \theta \cos \phi$, $m_x = \sin \theta \sin \phi$. With the effective shape anisotropy, the total energy of the system is

$$\mathcal{E} = \int [A|\nabla \mathbf{m}|^2 + K_z(\mathbf{m} \cdot \hat{\mathbf{z}})^2 - K_y(\mathbf{m} \cdot \hat{\mathbf{y}})^2 - M_s \mathbf{m} \cdot \mathbf{B}] dV + \int E_{\text{IDMI(BDMI)}} dV. \quad (\text{A1})$$

In spherical coordinates, the DMI energy density should be written as

$$E_{\text{IDMI}} = D_i \left(\sin^2 \theta \frac{\partial \phi}{\partial x} - \cos \phi \frac{\partial \theta}{\partial y} + \frac{\sin 2\theta}{2} \sin \phi \frac{\partial \phi}{\partial y} \right), \quad (\text{A2})$$

$$E_{\text{BDMI}} = D_b \left(-\sin^2 \theta \frac{\partial \phi}{\partial y} - \cos \phi \frac{\partial \theta}{\partial x} + \frac{\sin 2\theta}{2} \sin \phi \frac{\partial \phi}{\partial x} \right). \quad (\text{A3})$$

We introduce a Lagrangian representation [20] with kinetic term

$$\mathcal{L}_T = -\frac{M_s}{\gamma} \int \cos \theta \frac{\partial \phi}{\partial t} dV \quad (\text{A4})$$

and dissipation term

$$\mathcal{W} = \frac{M_s}{2\gamma} \int \left[\left(\frac{\partial \theta}{\partial t} \right)^2 + \sin^2 \theta \left(\frac{\partial \phi}{\partial t} \right)^2 \right] dV. \quad (\text{A5})$$

The Lagrangian is $\mathcal{L} = \mathcal{L}_T - \mathcal{E}$. The Euler-Lagrangian equations

$$\frac{d}{dt} \frac{\partial \mathcal{L}}{\partial (\partial_t q)} - \frac{\partial \mathcal{L}}{\partial q} = -\frac{\partial \mathcal{W}}{\partial (\partial_t q)} \quad (\text{A6})$$

reproduce the LLG Eq. (1), where L, W are integrands of \mathcal{L}, \mathcal{W} , and q represents θ or ϕ .

The CCM assumes the following planar Walker domain wall profile:

$$\theta(x, y, t) = 2 \arctan(e^{\frac{x-X(t)}{\Delta}}), \quad \phi(x, y, t) = \Phi(t), \quad (\text{A7})$$

with domain wall width

$$\Delta = \sqrt{\frac{A}{K_y + K_z \cos^2 \phi}}. \quad (\text{A8})$$

We further assume $K_z \ll K_y$ so the deformation of the domain wall is insignificant and $d\Delta/dt$ can be ignored. The 1D CCM model further assumes the magnetization is uniform in y and z directions. In the absence of DMI, the CCM for side-by-side domain walls is the same as the HtH/TtT or PMA walls, which has been well studied [20,38]. In the presence of BDMI, the 1D CCM Lagrangian and dissipation function can be obtained by substituting Eq. (A7) into \mathcal{L} and \mathcal{W} . For the nonconvergent integral $\int \cos \theta dx$, we consider the principal value $\lim_{L \rightarrow \infty} (\int_{-L}^L \cos \theta dx) = 2X$. Thus, we have

$$\mathcal{L} = dw \left(-2X \frac{M_s}{\gamma} \frac{d\Phi}{dt} + 2M_s B X \right) - \mathcal{E}_{\text{BDMI}}, \quad (\text{A9})$$

$$\mathcal{W} = \alpha dw \frac{M_s}{\gamma} \left[\frac{1}{\delta} \left(\frac{dX}{dt} \right)^2 + \Delta \left(\frac{d\Phi}{dt} \right)^2 \right]. \quad (\text{A10})$$

The equations of motion can be obtained by the Euler-Lagrangian equations with respect to $q = X$ and $q = \Phi$:

$$\frac{d}{dt} \frac{\partial \mathcal{L}}{\partial (\partial_t q)} - \frac{\partial \mathcal{L}}{\partial q} = -\frac{\partial \mathcal{W}}{\partial (\partial_t q)}. \quad (\text{A11})$$

We have

$$\frac{d\Phi}{dt} + \alpha \frac{1}{\Delta} \frac{dX}{dt} = \gamma B, \quad (\text{A12})$$

$$\frac{M_s}{\gamma} \left(\alpha \frac{d\Phi}{dt} - \frac{1}{\Delta} \frac{dX}{dt} \right) = K_z \sin 2\Phi - \frac{\pi D}{2\Delta} \sin \Phi. \quad (\text{A13})$$

For the rigid body motion, $\partial \Phi / \partial t = 0$, we have the relation

$$B = \frac{\alpha}{M_s} \left(K_z \sin 2\Phi - \frac{\pi D}{2\Delta} \sin \Phi \right). \quad (\text{A14})$$

Thus, the Walker breakdown field B_W is the maximal value of the right-hand side, above which the rigid body motion is invalid. This value can be calculated straightforwardly after some tedious mathematics. The results are plotted in the inset of Fig. 5(b).

In the presence of IDMI, we introduce a 2D CCM model by allowing $X = X(y, t)$. For simplicity, we assume $\partial X / \partial y = c$ is a constant. The CCM gives the domain wall energy Eq. (10) and the corresponding Lagrangian

$$\mathcal{L} = dw \left(-2X_0 \frac{M_s}{\gamma} \frac{d\Phi}{dt} + 2M_s B X_0 \right) - \mathcal{E}_{\text{IDMI}}, \quad (\text{A15})$$

where X_0 is the domain wall center position at $y = 0$ (the centerline of the strip). Notice that besides X_0 and Φ , c is also a variable and has its own Euler-Lagrangian equation $\partial \mathcal{L} / \partial c = 0$, giving

$$c = \frac{-\pi D_i \cos \Phi}{4\sqrt{A(K_y + K_z \cos^2 \Phi)}}. \quad (\text{A16})$$

The second equation of motion is modified as

$$\frac{M_s}{\gamma} \left(\alpha \frac{d\Phi}{dt} - \frac{1}{\Delta} \frac{dX}{dt} \right) = (1 + c^2) K_z \sin 2\Phi + \frac{\pi D c}{2\Delta} \sin \Phi. \quad (\text{A17})$$

We can similarly obtain the relation for rigid body motion:

$$B = \frac{\alpha}{M_s} \left[(1 + c^2) K_z \sin 2\Phi + \frac{\pi D c}{2\Delta} \sin \Phi \right]. \quad (\text{A18})$$

Substituting Eq. (A16) into the above relation, and taking the maximal value, we can find the breakdown field B_W for IDMI.

APPENDIX B: INFLUENCE OF INHOMOGENEOUS ANISOTROPY

Practically, the material may be inhomogeneous so the material parameters are position dependent. Here we briefly discuss the influence of inhomogeneous anisotropy K_u . We divide the 1536-nm-wide strip into 256 grains using Voronoi tessellation [35]. Each grain is assigned a random number r following the standard normal distribution and the anisotropy of the grain is $(1 + 0.1r)K_u$. A typical grain tessellation and the corresponding anisotropy distribution are shown in Fig. 8(a) (the brightness of the color encodes the anisotropy strength). Due to the inhomogeneous anisotropy, the generation of vortices becomes more complicated. Figure 8(b) shows the snapshots of domain wall dynamics at 16 ns and 19 ns under $B = 13.8$ mT. Different from Figs. 3(a) and 3(b), there are multiple two-vortex processes and vortices with different polarities coexisting. The total winding number is still 0. The direction of transverse motion of a vortex depends on the product of vorticity and polarity, as labeled in the figure. The average domain wall speed is smaller than the homogeneous sample. More domain wall dynamics in the presence of different kinds of defects and randomness will be studied in the future.

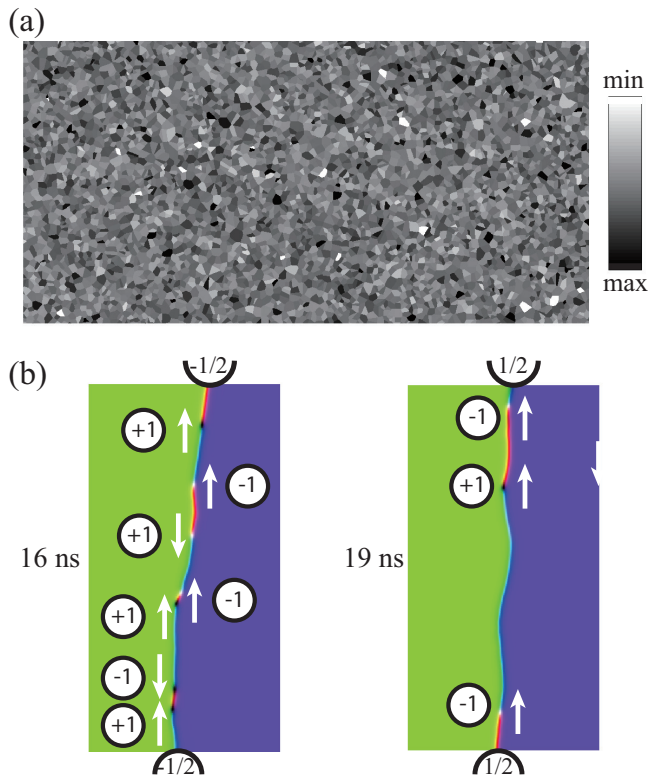


FIG. 8. (a) A typical grain tessellation and the corresponding anisotropy distribution (the gray-scale color bar). (b) Snapshots of domain wall dynamics at 16 ns and 19 ns under $B = 13.8$ mT.

APPENDIX C: DOMAIN WALL DYNAMICS IN THE PRESENCE OF DMI

We first discuss the BDMI. We observe similar solitonlike dynamics as Ref. [30]. Figure 9(a) shows close-up snapshots of a segment of domain wall. Due to the BDMI, the energy of vortices of opposite chirality becomes different and their transverse speed is also different. Here we denote the vorticity (1D winding number) by V , the polarity by P , and the skyrmion number (2D winding number) by Q . Then, for a local vortex, $Q = \frac{1}{2}VP$ [42,54]. At 2.90 ns, a $V = -1, P = -1$ antivortex collides with a $V = +1, P = +1$ vortex (indicated by the black circle). Then they annihilate and the spin wave is emitted (the spin wave ripple can be seen in the 2.92 ns snapshot). This procedure is different from that in the absence

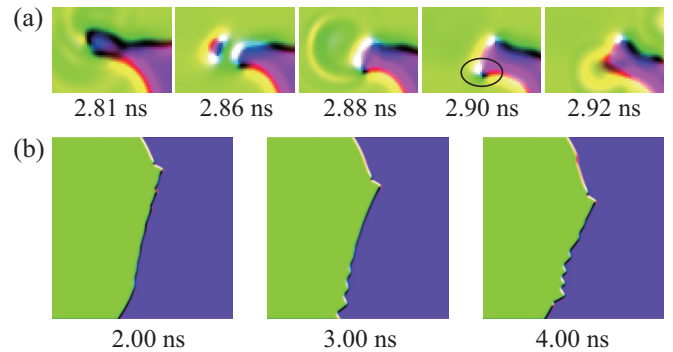


FIG. 9. (a) Close-up view of a segment of domain wall for $w = 1536$ nm, $D_b = 0.8$ mJ/m², and $B = 150$ mT. (b) Domain wall for $w = 1536$ nm, $D_i = 1.3$ mJ/m², and $B = 15.2$ mT.

of DMI. In the absence of DMI, the collision can only happen between a vortex ($V = +1$) and an antivortex ($V = -1$) of the same P who move in opposite directions. Both total V and total Q are conserved to be 0, and the annihilation is smooth with negligible spin wave emission. However, in the presence of BDMI, the $V = -1, P = -1$ antivortex, and the $V = +1, P = +1$ vortex have same $Q = +\frac{1}{2}$ and move in the same direction. V is conserved but Q is not conserved during the annihilation. Thus, significant spin-wave emission can be observed. We also identify another kind of spin-wave emission mechanism (we note that this can also be observed in the PMA case). See the 2.81 ns and 2.86 ns snapshots. A bubble of $Q = +1$ detaches from the domain wall due to the severe distortion. Then the bubble blasts, accompanied with significant spin wave emission (see the ripples in the 2.88 ns snapshot).

Then we discuss the IDMI. In the presence of IDMI, the domain wall becomes zigzag and the magnetization of the domain wall center is mainly out of plane except the transition regions between adjacent segments. The tilting direction of each segment follows the rule discussed in the main text for static domain walls. Zigzags gradually emerge at the edge and inside the long segments and annihilate at the middle. It can also be seen that compared to the fast vortex dynamics in the BDMI case (~ 0.1 ns), the zigzags' evolution is much slower. The zigzags are not local textures like vortices, but the transition regions can also be treated as vortices. We will study the dynamics of the local textures (solitons) from a statistical point of view in the future.

- [1] D. A. Allwood, G. Xiong, C. C. Faulkner, D. Atkinson, D. Petit, and R. P. Cowburn, Magnetic domain-wall logic, *Science* **309**, 1688 (2005).
- [2] S. S. P. Parkin, M. Hayashi, and L. Thomas, Magnetic domain-wall racetrack memory, *Science* **320**, 190 (2008).
- [3] B. Cullity and C. Graham, *Introduction to Magnetic Materials*, 2nd ed. (John Wiley & Sons, Inc., Hoboken, New Jersey, 2009).
- [4] N. L. Schryer and L. R. Walker, The motion of 180° domain walls in uniform dc magnetic fields, *J. Appl. Phys.* **45**, 5406 (1974).
- [5] G. S. D. Beach, C. Nistor, C. Knutson, M. Tsoi, and J. L. Erskine, Dynamics of field-driven domain-wall propagation in ferromagnetic nanowires, *Nat. Mater.* **4**, 741 (2005).
- [6] P. J. Metaxas, J. P. Jamet, A. Mougin, M. Cormier, J. Ferré, V. Baltz, B. Rodmacq, B. Dieny, and R. L. Stamps, Creep and Flow Regimes of Magnetic Domain-Wall Motion In ultrathin Pt/Co/Pt Films with Perpendicular Anisotropy, *Phys. Rev. Lett.* **99**, 217208 (2007).
- [7] X. S. Wang, P. Yan, Y. H. Shen, G. E. W. Bauer, and X. R. Wang, Domain Wall Propagation Through Spin Wave Emission, *Phys. Rev. Lett.* **109**, 167209 (2012).

- [8] S. Zhang and Z. Li, Roles of Nonequilibrium Conduction Electrons on the Magnetization Dynamics of Ferromagnets, *Phys. Rev. Lett.* **93**, 127204 (2004).
- [9] A. Thiaville, Y. Nakatani, J. Miltat, and Y. Suzuki, Micromagnetic understanding of current-driven domain wall motion in patterned nanowires, *Europhys. Lett.* **69**, 990 (2005).
- [10] A. Yamaguchi, T. Ono, S. Nasu, K. Miyake, K. Mibu, and T. Shinjo, Real-Space Observation of Current-Driven Domain Wall Motion in Submicron Magnetic Wires, *Phys. Rev. Lett.* **92**, 077205 (2004).
- [11] A. Brataas, A. D. Kent, and H. Ohno, Current-induced torques in magnetic materials, *Nat. Mater.* **11**, 372 (2012).
- [12] D. Hinzke and U. Nowak, Domain Wall Motion by the Magnonic Spin Seebeck Effect, *Phys. Rev. Lett.* **107**, 027205 (2011).
- [13] A. A. Kovalev and Y. Tserkovnyak, Thermomagnonic spin transfer and Peltier effects in insulating magnets, *Europhys. Lett.* **97**, 67002 (2012).
- [14] W. Jiang, P. Upadhyaya, Y. Fan, J. Zhao, M. Wang, L.-T. Chang, M. Lang, K. L. Wong, M. Lewis, Y.-T. Lin, J. Tang, S. Cherepov, X. Zhou, Y. Tserkovnyak, R. N. Schwartz, and K. L. Wang, Direct Imaging of Thermally Driven Domain Wall Motion in Magnetic Insulators, *Phys. Rev. Lett.* **110**, 177202 (2013).
- [15] X. S. Wang and X. R. Wang, Thermodynamic theory for thermal-gradient-driven domain-wall motion, *Phys. Rev. B* **90**, 014414 (2014).
- [16] P. Yan, X. S. Wang, and X. R. Wang, All-Magnonic Spin-Transfer Torque and Domain Wall Propagation, *Phys. Rev. Lett.* **107**, 177207 (2011).
- [17] J. Han, P. Zhang, J. T. Hou, S. A. Siddiqui, and L. Liu, Mutual control of coherent spin waves and magnetic domain walls in a magnonic device, *Science* **366**, 1121 (2019).
- [18] Y. Wang, D. Zhu, Y. Yang, K. Lee, R. Mishra, G. Go, S.-H. Oh, D.-H. Kim, K. Cai, E. Liu, S. D. Pollard, S. Shi, J. Lee, K. L. Teo, Y. Wu, K.-J. Lee, and H. Yang, Magnetization switching by magnon-mediated spin torque through an antiferromagnetic insulator, *Science* **366**, 1125 (2019).
- [19] G. Tatara and H. Kohno, Theory of Current-Driven Domain Wall Motion: Spin Transfer Versus Momentum Transfer, *Phys. Rev. Lett.* **92**, 086601 (2004).
- [20] J. Shibata, G. Tatara, and H. Kohno, A brief review of field- and current-driven domain-wall motion, *J. Phys. D* **44**, 384004 (2011).
- [21] H. Yuan and X. Wang, Birth, growth and death of an antivortex during the propagation of a transverse domain wall in magnetic nanostrips, *J. Magn. Magn. Mater.* **368**, 70 (2014).
- [22] V. Estévez and L. Laurson, Head-to-head domain wall structures in wide permalloy strips, *Phys. Rev. B* **91**, 054407 (2015).
- [23] T. Herranen and L. Laurson, Domain walls within domain walls in wide ferromagnetic strips, *Phys. Rev. B* **92**, 100405(R) (2015).
- [24] I. M. Miron, T. Moore, H. Szabolcs, L. D. Buda-Prejbeanu, S. Auffret, B. Rodmacq, S. Pizzini, J. Vogel, M. Bonfim, A. Schuhl, and G. Gaudin, Fast current-induced domain-wall motion controlled by the Rashba effect, *Nat. Mater.* **10**, 419 (2011).
- [25] S. Emori, U. Bauer, S.-M. Ahn, E. Martinez, and G. S. D. Beach, Current-driven dynamics of chiral ferromagnetic domain walls, *Nat. Mater.* **12**, 611 (2013).
- [26] J. Hütner, T. Herranen, and L. Laurson, Multistep Bloch-line-mediated walker breakdown in ferromagnetic strips, *Phys. Rev. B* **99**, 174427 (2019).
- [27] K. A. Hunnestad, E. D. Roede, A. T. J. van Helvoort, and D. Meier, Characterization of ferroelectric domain walls by scanning electron microscopy, *J. Appl. Phys.* **128**, 191102 (2020).
- [28] I. L. Prejbeanu, L. D. Buda, U. Ebels, and K. Ounadjela, Observation of asymmetric Bloch walls in epitaxial Co films with strong in-plane uniaxial anisotropy, *Appl. Phys. Lett.* **77**, 3066 (2000).
- [29] S. K. Vayalil, A. Koorikkatt, A. K. Gopi, S. V. Roth, and P. S. A. Kumar, Tailoring of uniaxial magnetic anisotropy in permalloy thin films using nanorippled Si substrates, *J. Phys.: Condens. Matter* **32**, 185804 (2020).
- [30] Y. Yoshimura, K.-J. Kim, T. Taniguchi, T. Tono, K. Ueda, R. Hiramatsu, T. Moriyama, K. Yamada, Y. Nakatani, and T. Ono, Soliton-like magnetic domain wall motion induced by the interfacial Dzyaloshinskii-Moriya interaction, *Nat. Phys.* **12**, 157 (2016).
- [31] B. N. Filippov, L. G. Korzunin, and F. A. Kassan-Ogly, Nonlinear dynamics of vortexlike domain walls in magnetic films with in-plane anisotropy in a pulsed magnetic field, *Phys. Rev. B* **70**, 174411 (2004).
- [32] F. Zhuo and Z. Z. Sun, Field-driven domain wall motion in ferromagnetic nanowires with bulk Dzyaloshinskii-Moriya interaction, *Sci. Rep.* **6**, 25122 (2016).
- [33] A. Thiaville, S. Rohart, É. Jué, V. Cros, and A. Fert, Dynamics of Dzyaloshinskii domain walls in ultrathin magnetic films, *Europhys. Lett.* **100**, 57002 (2012).
- [34] T. L. Gilbert, A phenomenological theory of damping in ferromagnetic materials, *IEEE Trans. Magn.* **40**, 3443 (2004).
- [35] A. Vansteenkiste, J. Leliaert, M. Dvornik, M. Helsen, F. Garcia-Sanchez, and B. Van Waeyenberge, The design and verification of MuMax3, *AIP Adv.* **4**, 107133 (2014).
- [36] A. Aharoni, Demagnetizing factors for rectangular ferromagnetic prisms, *J. Appl. Phys.* **83**, 3432 (1998).
- [37] A. Mougin, M. Cormier, J. P. Adam, P. J. Metaxas, and J. Ferré, Domain wall mobility, stability and walker breakdown in magnetic nanowires, *Europhys. Lett.* **78**, 57007 (2007).
- [38] A. Thiaville and Y. Nakatani, Domain-wall dynamics in nanowires and nanostrips, in *Spin Dynamics in Confined Magnetic Structures III*, edited by B. Hillebrands and A. Thiaville (Springer, Berlin, 2006), pp. 161–205.
- [39] X. Wang, P. Yan, J. Lu, and C. He, Magnetic field driven domain-wall propagation in magnetic nanowires, *Ann. Phys.* **324**, 1815 (2009).
- [40] See Supplemental Material at <http://link.aps.org/supplemental/10.1103/PhysRevB.106.014412> for the movies of domain wall dynamics corresponding to Figs. 3(a) and 3(b), respectively.
- [41] D. G. Porter and M. J. Donahue, Velocity of transverse domain wall motion along thin, narrow strips, *J. Appl. Phys.* **95**, 6729 (2004).
- [42] O. Tchernyshyov and G.-W. Chern, Fractional Vortices and Composite Domain Walls in Flat Nanomagnets, *Phys. Rev. Lett.* **95**, 197204 (2005).
- [43] A. A. Thiele, Steady-State Motion of Magnetic Domains, *Phys. Rev. Lett.* **30**, 230 (1973).
- [44] H. Y. Yuan and X. R. Wang, Nano magnetic vortex wall guide, *AIP Adv.* **5**, 117104 (2015).

- [45] O. Boulle, S. Rohart, L. D. Buda-Prejbeanu, E. Jué, I. M. Miron, S. Pizzini, J. Vogel, G. Gaudin, and A. Thiaville, Domain Wall Tilting in the Presence of the Dzyaloshinskii-Moriya Interaction in Out-Of-Plane Magnetized Magnetic Nanotracks, *Phys. Rev. Lett.* **111**, 217203 (2013).
- [46] K.-S. Ryu, S.-H. Yang, L. Thomas, and S. Parkin, Current-driven domain wall motion due to volume spin transfer torque in co/nl multilayer systems on au underlayer, *Jpn. J. Appl. Phys.* **55**, 093002 (2016).
- [47] O. M. Volkov, F. Kronast, C. Abert, E. S. O. Mata, T. Kosub, P. Makushko, D. Erb, O. V. Pylypovskyi, M.-A. Mawass, D. Sheka, S. Zhou, J. Fassbender, and D. Makarov, Domain-Wall Damping in Ultrathin Nanostripes with Dzyaloshinskii-Moriya Interaction, *Phys. Rev. Appl.* **15**, 034038 (2021).
- [48] N. Nagaosa and Y. Tokura, Topological properties and dynamics of magnetic skyrmions, *Nat. Nanotechnol.* **8**, 899 (2013).
- [49] B. Barbara, Magnetization processes in high anisotropy systems, *J. Magn. Magn. Mater.* **129**, 79 (1994).
- [50] P. Yan and G. E. W. Bauer, Magnonic Domain Wall Heat Conductance in Ferromagnetic Wires, *Phys. Rev. Lett.* **109**, 087202 (2012).
- [51] R. Wieser, E. Y. Vedmedenko, and R. Wiesendanger, Domain wall motion damped by the emission of spin waves, *Phys. Rev. B* **81**, 024405 (2010).
- [52] D. A. Gilbert, J. G. Ramírez, T. Saerbeck, J. Trastoy, I. K. Schuller, K. Liu, and J. de la Venta, Growth-induced in-plane uniaxial anisotropy in V_2O_3/Ni films, *Sci. Rep.* **7**, 13471 (2017).
- [53] K. Shibata, J. Iwasaki, N. Kanazawa, S. Aizawa, T. Tanigaki, M. Shirai, T. Nakajima, M. Kubota, M. Kawasaki, H. S. Park, D. Shindo, N. Nagaosa, and Y. Tokura, Large anisotropic deformation of skyrmions in strained crystal, *Nat. Nanotechnol.* **10**, 589 (2015).
- [54] X. S. Wang and X. R. Wang, Topology in magnetism, in *Chirality, Magnetism and Magnetoelectricity: Separate Phenomena and Joint Effects in Metamaterial Structures*, edited by E. Kamenetskii (Springer International Publishing, Cham, 2021), pp. 357–403.